



ELSEVIER

Contents lists available at ScienceDirect

# Micro and Nano Engineering

journal homepage: [www.journals.elsevier.com/micro-and-nano-engineering](http://www.journals.elsevier.com/micro-and-nano-engineering)

Research paper

## Microfluidic characterization of biomimetic membrane mechanics with an on-chip micropipette

Marianne Elias<sup>a,b</sup>, Adrien Dutoya<sup>a</sup>, Adrian Laborde<sup>a</sup>, Aurélie Lecestre<sup>a</sup>, Costanza Montis<sup>b</sup>,  
Lucrezia Caselli<sup>b</sup>, Debora Berti<sup>b</sup>, Barbara Lonetti<sup>c</sup>, Clément Roux<sup>c</sup>, Pierre Joseph<sup>a,\*</sup>

<sup>a</sup> LAAS-CNRS, Université de Toulouse, CNRS, UPS, INP, 31400 Toulouse, France

<sup>b</sup> CSGI and Department of Chemistry, University of Florence, Sesto Fiorentino 50019, Italy

<sup>c</sup> IMRCP, Université de Toulouse, CNRS, UPS, Toulouse, France

### ARTICLE INFO

#### Keywords:

Microfluidics  
Microfabrication  
Micropipette  
Lipid membranes  
Biophysics  
Nanoparticles

### ABSTRACT

The mechanic properties of cell membranes control many biological processes. The complexity of natural membranes is often dealt with by building synthetic vesicles (Giant Unilamellar Vesicles, GUVs), which can be thought as micron-sized minimal cells. Micropipette aspiration technique is the gold standard to characterize membrane mechanics, but it involves manual, long and tedious experiments. Microfluidics is perfectly suited to handle GUVs and permits in particular to conceive on-chip micropipettes for automated, systematic studies of membrane mechanical moduli. We developed a microfabrication process that enables obtaining the required 3-level channels including a micropipette in the intermediate level, with micrometric alignment, sufficiently low adhesion and roughness. We extended the theoretical analysis of micropipette, valid for cylindrical geometries that microfabrication does not allow, to the on-chip geometry, by considering the deformation of a vesicle in a square cross-section trap. We confirmed the validity of our approach thanks to systematic experiments performed on GUVs with well-characterized compositions: the obtained values of the membrane stretching modulus are in quantitative agreement with the literature. As a case study, we used our device to show that GUVs challenged with copolymer micelles, typically used for drug delivery, displayed a significantly decrease of the membrane stretching modulus, which could mediate internalization of these nanovectors. This study opens the path to systematic studies of the influence of physico-chemical environment on the mechanics of cell membranes.

### 1. Introduction

Complex biological processes occur at cell membranes, such as endocytosis and exocytosis, i.e. the internalization and expulsion of molecules and nano-objects from and out the cell, respectively. Synthetic simplified mimics have been developed over the years to disentangle the physico-chemical and biological mechanisms involved in the interaction occurring at this biological interfaces [1]. The simplest synthetic architectures mimicking cell boundaries are Giant Unilamellar Vesicles (GUVs), which are micron-scale capsules enclosed by a lipid bilayer membrane [2]. Microengineering, and in particular microfluidics, offers relevant tools to manipulate such objects [3]. Indeed, microsystems benefit from the possibility to control physical and chemical stimuli at small scale (comparable to that of cells), with low volume and sub-second response time, and with the opportunity that chips can be designed for the targeted functionality. A number of recent

studies have exploited these advantages along several axes: on-chip fabrication of GUV and more complex biomimetic assemblies (complex composition [4], asymmetric [5] or multi-compartment vesicles [6]); trapping and manipulation of vesicles and cells [7–10] to measure vesicle's response such as permeabilization induced by protein insertion [11] or by exposure to antibiotics [12].

An important subset of cell membrane properties is their mechanics: it governs cell ability to deform during its interaction with surrounding cells or particles, and can thus influence for instance nanoparticle engulfment by passive endocytosis. Helfrich described theoretically how the shape of a vesicle relates to its energy [13] and suggested experiments to extract mechanical moduli, from quantifying vesicle's deformation under fixed applied pressure for a known geometry. The different measurement methods to characterize membrane mechanics, such as shape fluctuations, micropipette aspiration and x-ray scattering, do not always lead to similar values of the membranes' moduli, so that

\* Corresponding author.

E-mail address: [pjoseph@laas.fr](mailto:pjoseph@laas.fr) (P. Joseph).

<https://doi.org/10.1016/j.mne.2020.100064>

Received 31 March 2020; Accepted 25 May 2020

2590-0072/ © 2020 The Authors. Published by Elsevier B.V. This is an open access article under the CC BY-NC-ND license (<http://creativecommons.org/licenses/by-nc-nd/4.0/>).

metrology tools are still needed [14]. The micropipette aspiration technique has become the gold standard method to extract the mechanical properties of a cell or vesicle [15,16]. It suffers however from serious limitations: experiments are tedious and low throughput. They require to manually find a vesicle undergoing sedimentation and apply a suction with a glass tube attached to a micromanipulator. In addition, the fluid surrounding the vesicle cannot be changed easily, which is problematic for studies on the impact of different chemical stimuli. In order to overcome these limitations, microfluidic approaches have been designed, detailed in the review by Dahl et al. [17]. Most of the designs are developed for cells, with the objective to realize a mechanical phenotyping, i.e. relate qualitatively the deformability of cell to its nature [18,19], or to test the influence of lipid composition on red blood cell mechanics [20,21]. These works clearly exploit the potential of microfluidic manipulation to probe membrane mechanics. However, a robust fabrication method to obtain the 3-dimensional required configuration, as well as quantitative analysis of vesicle deformation taking into account the actual chip and vesicle geometries, are still needed.

In this context, we developed a microfabrication strategy to fabricate on-chip micropipettes. The designs were similar to the ones developed by Liu and Lee [18], but with an approach enabling micrometric alignment. The most robust process flow involved silicon and glass multilevel etching, combining dry and wet etching, and bonding. For a quantitative analysis of properties, we extended the micropipette approach to the real geometry obtained by microfabrication, by computing analytically the area increase of a vesicle blocked in a square constriction, that we call “rounded-square”. Our method enabled to extract unbiased mechanical information on the vesicle. We measured the stretching modulus  $K_A$  of GUV with standard lipid composition and we obtained values compatible with the literature, which validated the approach. As first application of the devices to biologically relevant situations, we evidenced a significant decrease of  $K_A$  for GUV that have been incubated with polymer nanoparticles, typically used for drug vectorization [22].

## 2. Materials and methods

### 2.1. Chip design and principle

In order to characterize the mechanical properties of GUVs, a microfluidic chip should (1) steer the GUV to a confinement trap, (2) permit to characterize its deformation inside the microtrap upon pressure increase. Such functionality was achieved by designing a chip in the spirit of the one developed by Lee and Liu in 2014 [18]. It is composed of the following elements (see Fig. 1A): an inlet/outlet, two long channels coming from the inlet and going to the outlet, a trap and bypass channels in the middle way between the two inlet and outlet channels.

The GUVs sizes are of the order 10 to 40  $\mu\text{m}$ , to be physiologically relevant. Therefore, the trap width and height were set to be 10  $\mu\text{m}$  to be efficient without leading to a too high hydraulic resistance, and all the other channels widths and heights, where the GUVs circulate, were set to be 40  $\mu\text{m}$ . Generally, traditional glass micropipettes are cylinders and the objects propagate symmetrically as they are aspirated inside the micropipette. Likewise, to maintain the symmetric deformation, the trap was built in the middle height of the channels (see Fig. 1B).

An appropriate choice of the hydraulic resistance of each chip segment, fixed by setting their dimension, is crucial for the operation of the chip. For a channel with a square cross-section, the hydraulic resistance is:  $R = 28.4 \eta L \frac{1}{h^3}$  ( $\eta$  is the dynamic viscosity of the liquid,  $L$  is the length of the microfluidic channel and  $h$  is its height). In order to confine the GUV inside the trap, the bypass and trap hydraulic resistances were chosen equal:  $R_{bp} \approx R_T$ . It was a practical compromise for two reasons. First, if the bypass resistance was smaller than the trap's, the GUVs would prefer to go in the bypass instead of the traps, thus making the study almost impossible (very low probability to trap a GUV). On the other hand, having the bypass resistance higher than the one of the trap would promote overcrowding of GUVs in the trap. It could have led to either adhesion (on the wall and/or to the GUV trapped), or to new GUV arriving expelling the one trapped, preventing a full study of deformation.

The flow thus equally separated into the bypass and trap branches: an object arriving at the interception of the trap and the bypass had 50% chance to be trapped. As already mentioned, the lateral dimensions of the trap were fixed at 10  $\mu\text{m}$  in width and height. Its length was set to a minimum of 50  $\mu\text{m}$  in order to properly block GUV. With minimum lateral dimensions of the bypass also fixed (40  $\mu\text{m}$  not to block other GUVs), it led to a length of 1.3 cm for the bypass.

Once a GUV was trapped, it stopped the flow in the trap channel (the resistance of the trap became very high) and the other objects coming continued their way to the bypass through the outlet channels, without disturbing the trapped vesicle. In this situation, the pressure difference  $\Delta P$  applied on the trapped object corresponds to the viscous pressure drop inside the bypass channel. While the trap was blocked the chip operated a simple pressure divider (analogous to the voltage divider of electronics), so that  $\Delta P$  was fixed by  $\Delta P_{tot}$ , the total pressure difference applied to the chip, multiplied by the ratio of the bypass resistance to the total chip resistance:  $\Delta P = \Delta P_{tot} R_{bp} / (R_{bp} + R_{in} + R_{out})$ . Long inlet/outlet channels, with associated high resistance, permitted to control the required low level of pressure drop applied on the object with increased precision: in our typical experiments,  $\Delta P = \Delta P_{tot} / 5$ .

An increase of pressure led to the deformation of the trapped object, and more specifically to an increase of the length of the GUV entering the trap channel. An analysis of this deformation was used to characterize the mechanics of the trapped GUV, like in micropipette experiments. Details of the computation, and in particular extension of the classical cylindrical micropipette to our geometry, are given in

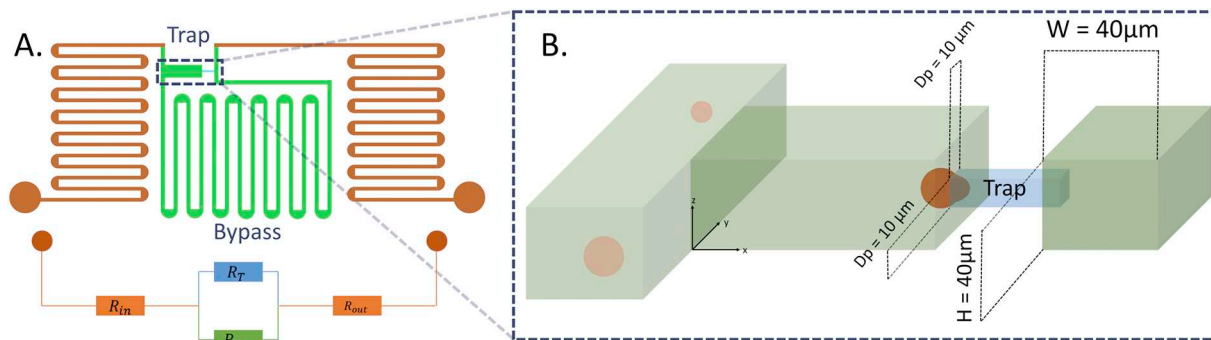


**Fig. 1.** A. Overview of fluidic chip design (not to scale). Bottom: scheme of hydraulic resistances. B. Configuration of the micropipette: flow separates into a bypass channel and a  $10 \times 10 \mu\text{m}^2$  square cross-section trap. Once a GUV is blocked, no more liquid flows into the trap and the vesicle is submitted to a pressure difference fixed by the viscous pressure drop in the bypass channel.

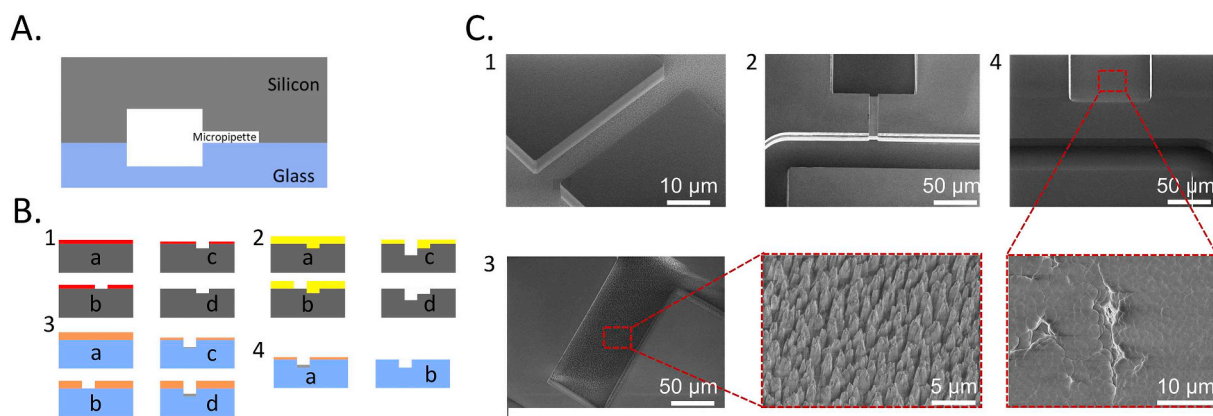


**Fig. 2.** A. Schematics of the architecture required to obtain a micropipette integrated in a microfluidic network (cross-section). B. Workflow for the silicon/glass chips etching. C. Characterization of the chips during fabrication (SEM pictures). (1) Micropipette plasma etching in silicon; (2) Bottom channel plasma etching in silicon, (3) Plasma etching of borofloat glass; (4) Glass wet etching to reduce roughness, followed by glass/silicon alignment, bonding and glass slide thinning.

**Section 3.1.** Before that, we describe in the next section the fabrication strategies we developed in order to fulfil design needs.

## 2.2. Fabrication of three-level chips in silicon-glass

As mentioned in the previous section, the chip design required a total channel height of 40  $\mu\text{m}$  and an intermediate 10  $\mu\text{m}$ -high trap level. Suitable imaging resolution required working with a high numerical aperture microscope objective. The associated working distance being small, the transparent substrate had to be thin (typically 170  $\mu\text{m}$ , the thickness of standard microscope coverslip). All the requirements mentioned above generated the necessity to fabricate a 3-layer microfluidic chip with the second one hanging in the middle of the two above and below with an alignment better than 10  $\mu\text{m}$ , as illustrated in Fig. 2A for the silicon-glass approach. Three different fabrication techniques were followed to answer these needs, each necessitating specific developments. The first two (PDMS-PDMS chips, and Dry Film chips techniques [23]) are described only in supplementary data, as they were finally discarded because of their respective limitations (difficulty of reproducible alignment, and adhesion issues). Therefore, we will only concentrate on the details of silicon-glass process that we developed to meet the requirements, and that was finally used to conduct our experiments. Masks were designed and drawn using Clewin software.

The technique used was etched Silicon channels, bonded on etched glass channels. This technique answered all the disadvantages we faced with PDMS and dry film. First, regarding alignment, glass and silicon are hardly deformable, which means their deformation was very low during the process. We used a glass type with the same thermal expansion coefficient as silicon, which prevented any misalignment upon heating or cooling. Second, the bonding process allowed sealing the two wafers with alignment accuracy better than 10  $\mu\text{m}$ . Moreover, for imaging glass is perfectly transparent and not auto-fluorescent at all. Finally, glass and silicon chemistry (mainly silanol groups) led to low GUV adhesion, and was suited for surface modification to decrease it further. The process is described in the following.

After silicon surface treatment and activation, a first photolithography followed by dry etching were realized in order to define the traps and the rest of the channels (see Fig. 2B and C, step 1). The dry plasma etching step was achieved using BOSCH process of alternative flow of  $\text{SF}_6/\text{C}_4\text{F}_8$  700/250 sccm at 10  $^\circ\text{C}$ : the first is to etch the Si and the second is to passivate the walls and protect them. To etch 10  $\mu\text{m}$ , we needed to expose 3 min and 20 s. After resist removal, a second photolithography/etching cycle was realized to etch the first part of the rest of channels (15  $\mu\text{m}$  depth for inlet, outlet and bypass), see Fig. 2B and C, step 2. A thicker resist (AZ<sup>®</sup> 40 XT, 20  $\mu\text{m}$ ) was needed in this step in order to fill the already etched trap. Plasma etching was achieved with

the same parameters as before, for 5 min to obtain 15  $\mu\text{m}$  depth. Fluid access holes were pierced using a sandblaster machine.

A specific process had to be developed for glass etching since sealing of the silicon and glass parts of the chip was performed with anodic bonding that required to work with non-purely silica glass (Borofloat B33, rich in  $\text{B}_2\text{O}_3$ ,  $\text{Na}_2\text{O}/\text{K}_2\text{O}$  and  $\text{Al}_2\text{O}_3$ , in our case). In particular, a specific adhesion layer (BARC<sup>™</sup> Bottom Anti-Reflecting Coating) was deposited before spin coating the photoresist and AZ<sup>®</sup> 15nXT (~17  $\mu\text{m}$  thickness) negative photoresist was used as protective layer. The plasma recipe was optimised to obtain the best resist and glass state after the etching. We tried two different process temperatures: at  $T = 20\text{ }^\circ\text{C}$  cracks formed in the resist mask, leading to similar defects in the glass wafer outside the desired zones. At  $T = -15\text{ }^\circ\text{C}$ , the resist did not fissure but we obtained rough etched glass. In order to avoid cracks but reduce this roughness, we worked at  $-15\text{ }^\circ\text{C}$  and divided the total time of etching in 9 cycles of 4 min 30 s each, in order to relax the resist constraints and clean the reactor after each cycle. The plasma process was realized using the following gases mix:  $\text{C}_4\text{F}_8/\text{CH}_4/\text{He}$ , 17/15/100 sccm, under  $4.8 \cdot 10^{-3}$  mbar, with source power and bias power respectively 2800 W and 250 W. However, plasma etching of a non-pure silica glass, containing in particular metallic compounds, caused non-homogeneous etching. The associated self-masking led to roughness of order 2  $\mu\text{m}$ , observed by mechanical profilometry and with SEM imaging (see Fig. 2C, step 3). It might have led to GUV adhesion, and could degrade the optical quality of microscopy imaging. Therefore, a complementary wet etching was done in (5% of HF 5%, 10% of HCl 37% and 85% of DI water). This etching was almost isotropic even for a material made of silica mixed with metallic impurities, which made the surface more polished. It typically reduced the roughness to less than around 100 nm peak-peak on a 100  $\mu\text{m}$  zone (see Fig. 2C, step 4).

The two etched wafers were then cleaned, aligned and sealed together by anodic bonding. The bonding machines we used permitted a precise enough optical alignment, that was made either before (for Suss wafer bonder) or after (for AML WB4 wafer bonder) heating. Standard bonding parameters were used: 370  $^\circ\text{C}$ , 4 mA current, 200 N force, 10 min.

Finally, high numerical microscope objectives used for high-resolution optics have a short working distance and are typically corrected for 170  $\mu\text{m}$ -thick glass coverslip, but the whole process had to be carried out on at least 500  $\mu\text{m}$ -thick glass wafers for mechanical manipulation. Consequently, an additional step of thinning and smoothing was made to reduce glass thickness from 500  $\mu\text{m}$  to 170  $\mu\text{m}$ . It consisted in Chemical Mechanical Polishing (Logitech PM5 machine). Several slurry liquids were sequentially used, consisting in aqueous suspensions of alumina particles with decreasing sizes 20  $\mu\text{m}$ , 6  $\mu\text{m}$ , 1  $\mu\text{m}$  at the different steps. The first two steps aimed at efficiently removing

materials, to decrease the wafer thickness. The third step (1  $\mu\text{m}$  diameter for the alumina particles), followed by a final polishing step with a softer plate and 0.3  $\mu\text{m}$  diameter Cerium oxide particles, enabled to obtain a low roughness surface (rms roughness  $r_q < 100$  nm), with optical quality suited for microscopy.

The processed wafer was finally cut into small chips containing each one four channels ready to be used.

## 2.3. Experimental

### 2.3.1. Vesicle preparation

Chemicals were purchased from Sigma Aldrich and Avanti Lipids. 1,2-dioleoyl-sn-glycero-3-phosphocholine (DOPC) lipid in powder was dissolved in Chloroform at 0.5 mg/mL concentrations. Lissamine rhodamine B sulfonyl (1,2-dimyristoyl-sn-glycero-3-phosphoethanolamine-N-) dye at 0.1% concentration of molecular number was added to the DOPC lipid solutions for fluorescence imaging. Before the experiment, a 10  $\mu\text{L}$  droplet of this solution was added in the centre of two ITO covered glasses. The two cover glasses were then placed under vacuum for two hours. We fabricated a homemade glass holder to fabricate the GUVs using the traditional electroformation technique [24]. Once the glasses were removed, one of them was placed in the holder, with an O-ring around the film. 200  $\mu\text{L}$  of 3 mM sucrose in water were added in the O-ring, before it was sealed with the second one. A sinusoidal voltage (peak-peak amplitude 2 V, frequency 10 Hz) was applied for 3 h on the film in order to fabricate the GUVs. The GUVs were then diluted 5 times in a 3 mM sucrose water solution.

### 2.3.2. Preparation and characterization of nanoparticles solution

Poly(ethylene oxide)-block-poly(caprolactone), PEO (5000  $\text{g}\cdot\text{mol}^{-1}$ )-PCL (5400  $\text{g}\cdot\text{mol}^{-1}$ ), micelles with a hydrodynamic diameter of  $25 \pm 5$  nm were prepared using a nanoprecipitation method. 20 mg of the copolymer were dispersed in 400  $\mu\text{L}$  of acetone and this solution was slowly added to 5 mL of a phosphate buffer (PBS) under stirring. Acetone was left to evaporate during 48 h. Dynamic Light Scattering measurements were performed at 25  $^\circ\text{C}$  and 173 $^\circ$  angle using a Malvern (Orsay, France) Zetasizer NanoZS to characterize the micelles' size. Data were analyzed using the general-purpose non-negative least squares (NNLS) method. The NP were diluted 50 times in DI water to obtain comparable osmolarity inside and outside the GUVs. The diluted GUVs and NP solutions were then mixed in a ratio 1:2 (GUVs: NP).

### 2.3.3. Microfluidic experiments

In order to connect the chip to the GUVs solution, we designed a chip holder with all the connectors integrated inside it. The two piece holders were 3D printed, using a high-resolution 3D printer (Dilase 3D, Kloe). A pressure controller (Fluigent MFSC – EZ, 0–69 mbar) was used to control the flow in the chip. The chip was pre-treated with an aqueous 0.5 mg/mL  $\beta$ -casein solution for 20 min, or equivalently with an aqueous 1% Bovine Serum Albumine (BSA) solution for 20 min, to reduce the adhesion of the GUVs on the walls of the channels. The GUVs solution was then sent in the chip, replacing all the casein (or BSA)

solution. Once a GUV was trapped, the pressure was fairly increased in order to pre-stress the object to eliminate possible defects. Then we decreased the pressure down to the one releasing the GUV from the trap: it defined experimentally the equilibrium pressure  $P_0$ , where the object started to get trapped. We started the deformation study by increasing the applied pressure difference by  $\Delta P_{\text{tot}} = 0.2$  mbar every 3 s, in order to leave enough time for the GUV to equilibrate at each pressure value. Upon each pressure increasing, the GUV was elongated inside the trap. Due to the pressure division imposed by the resistance, as described in Section 2.1, the corresponding increase of  $\Delta P$  on the object was 0.04 mbar. It corresponded to steps in membrane tension of order  $\Delta\tau \sim 0.02$   $\text{mN}\cdot\text{m}^{-1}$  for a 20  $\mu\text{m}$  vesicle (see eq. (1) below). The applied pressure was increased until the GUVs left the trap upon a certain pressure.

The images were acquired using a spinning disk microscope (Leica Microsystems), controlled with micromanager software. The wavelength used for excitation and emission for the GUVs membrane were  $\lambda_{\text{exc}} = 560$  nm and  $\lambda_{\text{em}} = 580$  nm. Image analysis was carried out using Image J software.

## 3. Results and discussion

### 3.1. Theory: extension of micropipette to realistic geometry

In order to extract quantitative mechanical parameters, we have generalized the computation used in micropipette experiment to our microchip geometry. In the following, we quickly summarize the standard cylindrical case, and describe its extension to a trap with square cross section.

#### 3.1.1. Principle of micropipette and computation for cylindrical geometry

The mechanics of a vesicle is described by the way its tension increases when its area increases. The micropipette technique uses two main ideas in order to determine the tension and area increase of a vesicle sucked at the entrance of a pipette: Laplace law, and volume conservation.

The first relationship is obtained by applying Laplace law, relating tension  $\tau$  to curvature, to the two interfaces located inside and outside the pipette, with the additional hypothesis that the vesicle is at mechanical equilibrium (homogeneous tension), and that the pressure inside it is homogeneous (implying in particular negligible flow). For a GUV of diameter  $D_v$  trapped in a cylindrical pipette of diameter  $D_p$ , submitted to a suction  $\Delta P$  (see Fig. 3A, 4A, or Fig. S4 in supplementary data), it finally reads:

$$\tau = \frac{\Delta P \cdot D_p}{4(1 - D_p/D_v)}. \quad (1)$$

The tension of the membrane can thus be deduced from the known imposed pressure difference, and the measured diameters of the GUV and pipette.

If we consider the conservation of the vesicle's volume during the experiment, we can deduce its area increase  $\Delta A$  between a reference

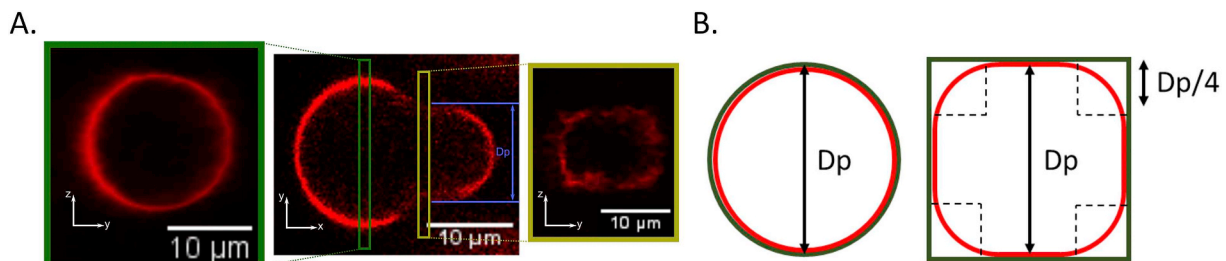


**Fig. 3.** Different configurations of micropipette experiments. (A) Experimental cross section of the vesicle perpendicular to the axis X of the pipette (left and right pictures, in the YZ plane), and along the axis X of the pipette (middle picture, in the XY plane). (B). Cross section perpendicular to the pipette for cylindrical and square geometries.

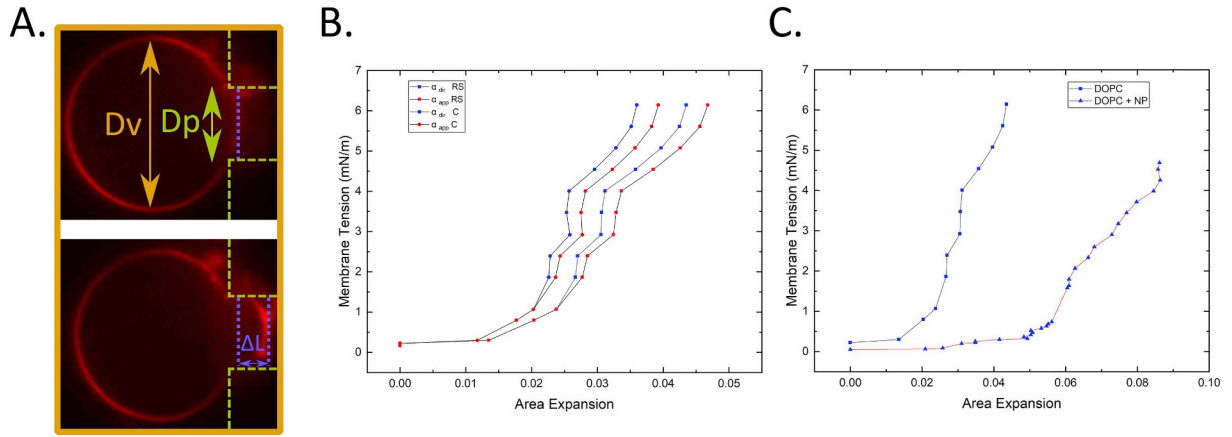


**Fig. 4.** Experimental results: A. images of the elongation  $\Delta L$  inside the trap, when increasing progressively the pressure. B. Membrane tension of DOPC GUVs as function of the apparent and direct area expansion for the cylindrical and rounded square shape. C. Membrane tension and direct area expansion for DOPC vesicles, and for DOPC incubated with nanoparticles.

state and a state in which its “tongue” extends by an additional length  $\Delta L$  within the pipette. Geometrical considerations lead to the following formula, after a first order Taylor expansion valid with a large vesicle (i.e.  $\Delta L D_p^2 \ll D_v^3$ ):

$$\Delta A = \pi D_p \Delta L \left[ 1 - \frac{D_p}{D_v} \right] \quad (2)$$

In summary, measuring  $\Delta L$ ,  $D_p$ ,  $D_v$  is an experimental way to determine the relationship between  $\Delta A$  and  $\tau$ . It should be compared with predictions to extract mechanical moduli. The theoretical analysis identifies two regimes. In the low-tension regime ( $\tau < 0.5 \text{ mN} \cdot \text{m}^{-1}$ ), the apparent relative area increase  $\alpha_{app} = \frac{\Delta A}{A_0}$  corresponds to the smoothing of microscopic thermal undulations [25,26], and is thus driven by the bending modulus  $\kappa_c$ :

$$\alpha_{app} = \frac{\Delta A}{A_0} = \frac{kT}{8\pi\kappa_c} \ln(\tau/\tau_0) \quad (3)$$

where  $k$  is Boltzmann constant,  $T$  the temperature,  $A_0$  the initial reference area, and  $\tau_0$  the initial tension. For higher values of tension (typically  $\tau > 1 \text{ mN} \cdot \text{m}^{-1}$ ), the apparent area per molecule increases linearly with the tension, defining the apparent stretching modulus  $K_{app}$  ( $\tau = K_{app}\alpha_{app}$ ). However, this apparent increase is a combination of the direct area increase per molecule and the remaining smoothing of undulations. Consequently, for the experimental determination of the direct stretching modulus  $K_{dir}$ , the thermal undulations (contribution of the bending modulus to the apparent area increase) need to be subtracted. As detailed in reference [27],  $K_{dir}$  is thus deduced by fitting the slope of the direct area increase  $\alpha_{dir}$ :  $\tau = K_{dir}\alpha_{dir}$ , where  $\alpha_{dir}$  is deduced for each  $i$ -th experimental value from the formula:

$$\alpha_{dir}(i) = \frac{\Delta A(i)}{A_0} - \frac{kT}{8\pi\kappa_c} \ln(\tau(i)/\tau(1)) \quad (4)$$

$\tau(1)$  is the initial tension state of the high-tension regime (fixed in our case to  $1 \text{ mN} \cdot \text{m}^{-1}$ ).

### 3.1.2. Extension to the “rounded-square” geometry corresponding to real fabricated designs

For our chips, but also for the one used in the work of Liu and Lee [18], the pipette did not have a cylindrical geometry, but rather a square cross-section. Consequently, the deformation of a GUV entering the trap is likely not to follow the previous relationship (2). In this work, we analyse the geometry of the vesicle and obtain an analytical formula to deduce quantitatively tension and area increase from experiments, for the on-chip micropipette. Let us point out that most fabrication approaches, inherently layer-by-layer, lead to this type of

shape, so that extending the cylindrical case to this one can be of significant interest.

We focus on the actual vesicle geometry when entering a pipette with square cross-section (trap channel). We consider that the extremity of the vesicle in the trap adopts a half-sphere shape, which is the simplest constant curvature shape, with a diameter equal to the width of the pipette  $D_p$ , also equal to its height. Since Eq. (1) has been obtained for the cylindrical case by equating the Laplace pressure jump on the upstream and downstream sides, that have similar curvatures for the rounded-square shape and for the cylindrical cases, this relation still holds for the rounded-square geometry, where the cylinder diameter just needs being replaced by the pipette width (or height).

However, contrary to the cylindrical case, the part of the vesicle extending along the walls of the traps cannot totally be in contact with the walls because of sharp corners (see Fig. 3B or Fig. S4 in supplementary data). It results in the presence of liquid surrounding it, connected to the downstream trap channel. Mechanical equilibrium of this part of the vesicle with the hemispherical cap (downstream trap side) leads to a shape that we call “rounded square”, the geometry of which is shown in Fig. 3B. It consists in flat portions in the middle of each channel face, connected by quarters of cylinders in the corners. Briefly, equating the tension and pressure jump along the walls and on the hemispherical cap fixes  $r_c$ , the radius of curvature of the part of the vesicle that does not touch the walls (the corners) to:  $r_c = D_p/4$ . This non-cylindrical shape modifies the way the surface area increases when the length of the tongue present in the trap increases. Geometrical computation, taking into account volume conservation, and a Taylor expansion similar to the cylindrical case, leads to:

$$\Delta A = \left( 2 + \frac{\pi}{2} \right) D_p \Delta L \left[ 1 - 4 \frac{D_p}{D_v} \cdot \frac{\frac{3}{4} + \frac{\pi}{16}}{2 + \frac{\pi}{2}} \right]. \quad (5)$$

Details of computations, as well as the exact formula (before the Taylor expansion) are given in Supplementary data.

We can note that the first term  $\left( 2 + \frac{\pi}{2} \right) D_p \Delta L$  corresponds to the area of the vesicle inserted within the pipette (rounded square perimeter multiplied by tongue length), whereas the additional one (term proportional to  $D_p/D_v$  in the bracket) accounts for the diminution of the upstream vesicle area. Eq. (5), even if similar in its form to eq. (2) in the way area increase relates to measured length, differs by its numerical factors, and should be used to properly extract mechanical moduli from the experiments.

### 3.2. Application to characterizing the mechanics of membranes

In order to validate our chips, as well as the geometrical considerations developed in Section 3.1, we measured the progressive deformation of vesicles with a well-characterized composition. Electroformed DOPC vesicles were captured and their deformation upon pressure increase was characterized, following the experimental procedure described in Section 2.3. The successive shapes of a vesicle upon pressure increase ( $\Delta L$  as function of  $\Delta P$ ) were captured by confocal microscopy, as shown in Fig. 4A. We focused on the large deformation regime, for which the GUV extended more in the pipette. As  $\Delta P/\Delta P_{tot}$  was set to 1/5, the experimental resolution on pressure control only allow precise enough characterization at tension higher than 0.1 mN.m<sup>-1</sup>. However our approach can be used to study the low-tension regime, by designing chips with more drastic pressure division  $\Delta P/\Delta P_{tot}$ , see Section 2.1. We thus fixed the bending modulus, required in order to deduce  $\alpha_{dir}$ , from the literature:  $\kappa_b = 8.5 \cdot 10^{-20}$  J [27]. As described in Section 3, we plot in Fig. 4B the evolution of  $\tau$  as function of the apparent and direct area expansion with two hypothesis: a cylindrical geometry (C label, eqs. (1) and (2)), or a rounded-square one (RS label, Eqs. (1) and (5)).

By fitting in Fig. 4B the slope of  $\tau$  vs  $\alpha_{app}$ , and  $\tau$  vs  $\alpha_{dir}$  (eq. 4), we could deduce the apparent and direct stretching moduli for DOPC membranes. We obtained (average on measurements on two vesicles)  $K_{app} = 228 \pm 27$  mN.m<sup>-1</sup> and  $K_{dir} = 257 \pm 36$  mN.m<sup>-1</sup>, the error bar being the standard deviation. The values obtained for pure DOPC vesicles, with the rounded-square hypothesis, is fully compatible with the literature [27,28]. It is significantly different (15% lower) from the one that would have been deduced from a cylindrical hypothesis, as demonstrated by the deviation between C and RS curves in Fig. 4B.

In order to assess the ability of our chips to discriminate between GUV with different mechanical properties, we tested the effects of nanoparticles on membrane mechanics, by probing GUV of equal composition (pure DOPC) that had been incubated for half an hour with a solution containing nanoparticles (NP) before sending them into the chip. The NP were self-assembled polymer micelles, developed for drug vectorization due to their ability to solubilize hydrophobic compounds. Fig. 4C demonstrates that the NP led to a very significant decrease of the GUV membrane stretching modulus, down to a value of  $K_{app} = 110 \pm 15$  mN.m<sup>-1</sup>, and  $K_{dir} = 112 \pm 15$  mN.m<sup>-1</sup> (using the tabulated bending modulus of pure DOPC lipid). In that case, the error bar was estimated from the accuracy of the fitting, since the standard deviation of the measurements we made was smaller (2.5 mN.m<sup>-1</sup>). A possible origin of this decreased stretching modulus of the DOPC vesicles is that upon interaction of the PEO-PCL micelles, the micelles (partly) merge with the lipid bilayer, which could lead to  $K_{app}$  values intermediate between that of DOPC and that of pure PEO-PCL vesicles. Typical values of the stretching modulus of membranes made of amphiphilic copolymer in the literature are indeed below 100 mN.m<sup>-1</sup>, (for example, for pure PEO-PBD membrane,  $K_{app} = 89$  mN.m<sup>-1</sup> in reference [29]). The decrease of measured  $K_{app}$  could also originate from the fact that these nanovectors create defects in the membrane, modifying the effective stretching modulus. This is consistent with experiments on Large Unilamellar Vesicles (LUV) in the absence or presence of polymer micelles where PEO-PCL micelles increased the permeability of DOPC LUV (see Fig. S4 in supplementary data).

It is also worth noting that this mixture also allowed a quite large maximum area increase, superior to 8%, whereas lipid membranes are usually known to rupture for an increase of order 5%. These two elements (lowered stretching modulus and ability to reach high deformations) could play an important role in the potential of such NP to interact efficiently with membranes, a key asset for drug carriers.

A drawback of the rounded-square geometry is the presence of a slight residual flow in the corner of the square pipette. We observed however that this residual flow was significant only for GUV of size very close to the trap dimension ( $D_v \sim D_p$ ), whereas large vesicles (in the

order of 20  $\mu$ m diameter for a 10  $\mu$ m-wide trap) completely blocked the flow inside the pipette. As perspective, adapting the geometry to situation combining trapping with a residual flow could be turned into an advantage, to study for example how a shear stress is transmitted across the membrane [30], or how shear affects lipid domain dynamics [31]. In relation to nanomedicine applications, it would also open the path to investigating how a shear flow applied to the membrane can enhance nano-objects internalization, or influence drug release by such nano-carriers.

## 4. Conclusion

We have developed a technological method to fabricate on-chip micropipettes, suited to complex multilevel geometry with alignment. We have extended the computation of micropipette to geometry corresponding to the ones accessible by microfabrication. The approach has been quantitatively validated by extracting values of the stretching modulus for known composition of the vesicle's membrane. As original application of the device, we have demonstrated that polymer nanoparticles significantly influences membrane mechanics. Future work includes systematic study of the effect of nanoparticles on mechanical moduli. With respect to the standard micropipette, the on-chip format benefits from several advantages: trapping is spontaneous obtained without manual micromanipulation step of GUV. The microfluidic approach also permits to diversify chip design to integrate other functionalities in the future: parallel measurements by multiplexing pipettes, dynamic chemical stimuli by combining traps with an upstream Y junction, in order to probe the effect of exposure to different chemicals.

## Declaration of Competing Interest

None.

## Acknowledgements

This work was supported in part by CNRS through the PICS CNRS 2016-2019 program "Microfluidics for Soft Matter", and by INSIS-CNRS. This work was partly supported by LAAS-CNRS micro and nanotechnologies platform member of the French RENATECH network. We thank Fabien Mesnilgrete, Laurent Mazenq, and Samuel Charlot for help in the microfabrication process, Rémi Courson for the 3D chip-holder fabrication (Multifab project), Sandrine Souleille for help in microfluidic instrumentation, Julien Roul for help in confocal imaging, and Elouan Ronjon for the leakage experiments.

## Appendix A. Supplementary data

Supplementary data to this article can be found online at <https://doi.org/10.1016/j.mne.2020.100064>.

## References

- [1] T.J. Lagny, P. Bassereau, Bioinspired membrane-based systems for a physical approach of cell organization and dynamics: usefulness and limitations, *Interface Focus* 5 (2015) 20150038, <https://doi.org/10.1098/rsfs.2015.0038>.
- [2] K. Kamiya, S. Takeuchi, Giant liposome formation toward the synthesis of well-defined artificial cells, *J. Mater. Chem. B* 5 (2017) 5911–5923, <https://doi.org/10.1039/C7TB01322A>.
- [3] M. Zagnoni, Miniaturised technologies for the development of artificial lipid bilayer systems, *Lab Chip* 12 (2012) 1026–1039, <https://doi.org/10.1039/C2LC20991H>.
- [4] M. Sobrinos-Sanguino, S. Zorrilla, C.D. Keating, B. Monterroso, G. Rivas, Encapsulation of a compartmentalized cytoplasm mimic within a lipid membrane by microfluidics, *Chem. Commun.* 53 (2017) 4775–4778, <https://doi.org/10.1039/C7CC01289F>.
- [5] P.C. Hu, S. Li, N. Malmstadt, Microfluidic fabrication of asymmetric Giant lipid vesicles, *ACS Appl. Mater. Interfaces* 3 (2011) 1434–1440, <https://doi.org/10.1021/am101191d>.
- [6] T. Trantidou, M. Friddin, Y. Elani, N.J. Brooks, R.V. Law, J.M. Seddon, O. Ces, Engineering compartmentalized biomimetic micro- and Nanocontainers, *ACS Nano*

- 11 (2017) 6549–6565, <https://doi.org/10.1021/acsnano.7b03245>.
- [7] J. Nilsson, M. Evander, B. Hammarström, T. Laurell, Review of cell and particle trapping in microfluidic systems, *Anal. Chim. Acta* 649 (2009) 141–157, <https://doi.org/10.1016/j.aca.2009.07.017>.
- [8] W.-H. Tan, S. Takeuchi, A trap-and-release integrated microfluidic system for dynamic microarray applications, *PNAS*. 104 (2007) 1146–1151, <https://doi.org/10.1073/pnas.0606625104>.
- [9] A. Yamada, S. Lee, P. Bassereau, C.N. Baroud, Trapping and release of giant unilamellar vesicles in microfluidic wells, *Soft Matter* 10 (2014) 5878–5885, <https://doi.org/10.1039/C4SM00065J>.
- [10] C. Magnani, C. Montis, G. Mangiapia, A.-F. Mingotaud, C. Mingotaud, C. Roux, P. Joseph, D. Berti, B. Lonetti, Hybrid vesicles from lipids and block copolymers: phase behavior from the micro- to the nano-scale, *Colloids Surf. B: Biointerfaces* 168 (2018) 18–28, <https://doi.org/10.1016/j.colsurfb.2018.01.042>.
- [11] T. Robinson, P. Kuhn, K. Eyer, P.S. Dittrich, Microfluidic trapping of giant unilamellar vesicles to study transport through a membrane pore, *Biomicrofluidics*. 7 (2013) 044105, , <https://doi.org/10.1063/1.4816712>.
- [12] K.A. Nahas, J. Cama, M. Schaich, K. Hammond, S. Deshpande, C. Dekker, M.G. Ryadnov, U.F. Keyser, A microfluidic platform for the characterisation of membrane active antimicrobials, *Lab Chip* 19 (2019) 837–844, <https://doi.org/10.1039/C8LC00932E>.
- [13] W. Helfrich, Elastic properties of lipid bilayers: theory and possible experiments, *Z. Naturforsch. C* 28 (1973) 693–703.
- [14] D. Bochicchio, L. Monticelli, Chapter five - the membrane bending Modulus in experiments and simulations: A puzzling picture, in: A. Iglič, C.V. Kulkarni, M. Rappolt (Eds.), *Advances in Biomembranes and Lipid Self-Assembly*, Academic Press, 2016, pp. 117–143, , <https://doi.org/10.1016/bs.abl.2016.01.003>.
- [15] R. Waugh, E.A. Evans, Thermoelasticity of red blood cell membrane, *Biophys. J.* 26 (1979) 115–131 <https://www.ncbi.nlm.nih.gov/pmc/articles/PMC1328507/> (accessed September 11, 2018).
- [16] Evan. Evans, David. Needham, Physical properties of surfactant bilayer membranes: thermal transitions, elasticity, rigidity, cohesion and colloidal interactions, *J. Phys. Chem.* 91 (1987) 4219–4228, <https://doi.org/10.1021/j100300a003>.
- [17] J.B. Dahl, J.-M.G. Lin, S.J. Muller, S. Kumar, Microfluidic strategies for understanding the mechanics of cells and cell-mimetic systems, *Annual Review of Chemical and Biomolecular Engineering*. 6 (2015) 293–317, <https://doi.org/10.1146/annurev-chembioeng-061114-123407>.
- [18] L.M. Lee, A.P. Liu, A microfluidic pipette array for mechanophenotyping of cancer cells and mechanical gating of mechanosensitive channels, *Lab Chip* 15 (2014) 264–273, <https://doi.org/10.1039/C4LC01218F>.
- [19] L.M. Lee, J.W. Lee, D. Chase, D. Gebrezgiabhier, A.P. Liu, Development of an advanced microfluidic micropipette aspiration device for single cell mechanics studies, *Biomicrofluidics*. 10 (2016) 054105, , <https://doi.org/10.1063/1.4962968>.
- [20] Q. Guo, S.P. Duffy, K. Matthews, A.T. Santos, M.D. Scott, H. Ma, Microfluidic analysis of red blood cell deformability, *J. Biomech.* 47 (2014) 1767–1776, <https://doi.org/10.1016/j.jbiomech.2014.03.038>.
- [21] J. Kim, H. Lee, S. Shin, Advances in the measurement of red blood cell deformability: a brief review, *Journal of Cellular Biotechnology*. 1 (2015) 63–79, <https://doi.org/10.3233/JCB-15007>.
- [22] M. Dionzou, A. Morère, C. Roux, B. Lonetti, J.-D. Marty, C. Mingotaud, P. Joseph, D. Goudounèche, B. Payré, M. Léonetti, A.-F. Mingotaud, Comparison of methods for the fabrication and the characterization of polymer self-assemblies: what are the important parameters? *Soft Matter* 12 (2016) 2166–2176, <https://doi.org/10.1039/C5SM01863C>.
- [23] R. Courson, S. Cargou, V. Conedera, M. Fouet, M.C. Blatche, C.L. Serpentine, A.M. Gue, Low-cost multilevel microchannel lab on chip: DF-1000 series dry film photoresist as a promising enabler, *RSC Adv.* 4 (2014) 54847–54853, <https://doi.org/10.1039/C4RA09097G>.
- [24] M.I. Angelova, D.S. Dimitrov, Liposome electroformation, *Faraday Discuss. Chem. Soc.* 81 (1986) 303–311, <https://doi.org/10.1039/DC9868100303>.
- [25] E. Evans, W. Rawicz, Entropy-driven tension and bending elasticity in condensed-fluid membranes, *Phys. Rev. Lett.* 64 (1990) 2094–2097, <https://doi.org/10.1103/PhysRevLett.64.2094>.
- [26] P. Bassereau, B. Sorre, A. Lévy, Bending lipid membranes: experiments after W. Helfrich's model, *Adv. Colloid Interf. Sci.* 208 (2014) 47–57, <https://doi.org/10.1016/j.cis.2014.02.002>.
- [27] L. Lu, W.J. Doak, J.W. Schertzer, P.R. Chiarot, Membrane mechanical properties of synthetic asymmetric phospholipid vesicles, *Soft Matter* 12 (2016) 7521–7528, <https://doi.org/10.1039/C6SM01349J>.
- [28] W. Rawicz, K.C. Olbrich, T. McIntosh, D. Needham, E. Evans, Effect of chain length and unsaturation on elasticity of lipid bilayers, *Biophys. J.* 79 (2000) 328–339, [https://doi.org/10.1016/S0006-3495\(00\)76295-3](https://doi.org/10.1016/S0006-3495(00)76295-3).
- [29] J. Gaspard, L.M. Casey, M. Rozin, D.J. Munoz-Pinto, J.A. Silas, M.S. Hahn, Mechanical characterization of hybrid vesicles based on linear poly (Dimethylsiloxane-b-ethylene oxide) and poly(butadiene-b-ethylene oxide) block copolymers, *Sensors*. 16 (2016) 390, <https://doi.org/10.3390/s16030390>.
- [30] B. Sebastian, T. Favero, P.S. Dittrich, The effects of shear force transmission across vesicle membranes, *J. Phys. Chem. Lett.* 8 (2017) 6128–6134, <https://doi.org/10.1021/acs.jpcclett.7b02676>.
- [31] F. Sturzenegger, T. Robinson, D. Hess, P.S. Dittrich, Membranes under shear stress: visualization of non-equilibrium domain patterns and domain fusion in a microfluidic device, *Soft Matter* 12 (2016) 5072–5076, <https://doi.org/10.1039/C6SM00049E>.